Inverse Modeling of One-Dimensional Setup and Alongshore Current in the Nearshore

FALK FEDDERSEN AND R. T. GUZA

Scripps Institution of Oceanography, La Jolla, California

STEVE ELGAR

Woods Hole Oceanographic Institution, Woods Hole, Massachusetts

(Manuscript received 28 April 2003, in final form 28 July 2003)

ABSTRACT

Inverse models are developed that use data and dynamics to estimate optimally the breaking-wave-driven setup and alongshore current, as well as the cross-shore forcing, alongshore forcing, and drag coefficient. The inverse models accurately reproduce these quantities in a synthetic barred-beach example. The method is applied to one case example each from the Duck94 and SandyDuck field experiments. Both inverse solutions pass consistency tests developed for the inverse method and have forcing corrections similar to a roller model and significant cross-shore variation of the drag coefficient. The inverse drag coefficient is related to the wave dissipation, a bulk measure of the turbulence source, but not to the bed roughness, consistent with the hypothesis that breaking-wave-generated turbulence increases the drag coefficient. Inverse solutions from a wider range of conditions are required to establish the generality of these results.

1. Introduction

Models for breaking-wave-driven nearshore circulation often are based on the depth-integrated, time-averaged, and constant-density Navier–Stokes equations and are simplified by assuming that all variables are independent of the alongshore coordinate y and time (i.e., steady). The cross-shore momentum equation becomes a one-dimensional (1D) balance between the cross-shore pressure gradient and the total (wind plus wave) cross-shore forcing F_x (e.g., Longuet-Higgins and Stewart 1964):

$$-gh\frac{d\overline{\eta}}{dx} + F_x = 0, \tag{1}$$

where g is gravitational acceleration, h is the water depth, x is the cross-shore coordinate, and $\overline{\eta}$ is the time-averaged free surface elevation relative to mean sea level without waves (i.e., setup).

The alongshore momentum equation is a 1D balance between the alongshore forcing F_y, bottom stress, and lateral mixing (e.g., Longuet-Higgins 1970):

$$F_y - c_d\langle|\mathbf{u}|v\rangle + \frac{d}{dx}\left(\nu h\frac{d\overline{v}}{dx}\right) = 0, \tag{2}$$

where $\overline{v}$ is the mean (time and depth averaged) alongshore current. The second term in (2) is a common bottom stress representation (Longuet-Higgins 1970; Thornton and Guza 1986; Garcez-Faria et al. 1998; and many others), where c_d is a nondimensional drag coefficient, $\langle\rangle$ represents a time average over many wave periods, $|\mathbf{u}|$ is the total instantaneous horizontal velocity vector, and v is the instantaneous alongshore velocity. Mean and wave-orbital velocities contribute to $\langle|\mathbf{u}|v\rangle$. The third term in (2) represents lateral mixing processes (ν is an eddy viscosity) including shear dispersion (Svendsen and Putrevu 1994), shear waves (Slinn et al. 1998; Özkan-Haller and Kirby 1999), and small-scale turbulent mixing by breaking waves (Battjes 1975). The cross- and alongshore forcings are the sum of wind (τ_x^{wind} and τ_y^{wind}) and wave forcing and are given by

$$F_x = \rho^{-1}\left(\tau_x^{\text{wind}} - \frac{dS_{xx}}{dx}\right) \quad \text{and}$$

$$F_y = \rho^{-1}\left(\tau_y^{\text{wind}} - \frac{dS_{yx}}{dx}\right),$$

where ρ is the water density and S_{xx} and S_{yx} are components of the radiation stress tensor (Longuet-Higgins and Stewart 1964).

The 1D setup [(1)] and alongshore current [(2)] dynamics are applicable to many laboratory and field situations (e.g., Bowen et al. 1968; Battjes and Stive 1985; Thornton and Guza 1986; and many others). Although simple,

Corresponding author address: Dr. Falk Feddersen, Scripps Institution of Oceanography 0209, 9500 Gilman Dr., La Jolla, CA 92093-0209.
E-mail: falk@coast.ucsd.edu

except for the pressure gradient term, the functional forms of the terms in (1) and (2) are not known and must be parameterized for use in models. Linear theory relates the wave forcing to the root-mean-square (rms) wave height $H_{\rm rms}$, mean wave angle $\overline{\theta}$, and mean frequency $\overline{f}$, quantities predicted by bulk wave transformation models (e.g., Thornton and Guza 1983). However, linear-theory-based surf-zone wave-forcing parameterizations are not sufficiently accurate for detailed alongshore current modeling on a barred beach (Church and Thornton 1993; Reniers and Battjes 1997; Ruessink et al. 2001). An additional water column stress due to the aerated front face of a broken wave (wave roller) has been hypothesized to shift the wave forcing shoreward. This concept is applied in heuristic roller models (e.g., Stive and de Vriend 1994) based on towed wavefoil experiments (Duncan 1981). Inclusion of a roller model with tuned parameters results in improved agreement with observations on barred laboratory ($\overline{\eta}$ and $\overline{v}$; Reniers and Battjes 1997) and natural ($\overline{v}$; Ruessink et al. 2001) beaches.

The closure of 1D integrated alongshore momentum balances on cross-shore transects (Feddersen et al. 1998; Feddersen and Guza 2003) suggests that $c_d\langle|\mathbf{u}|v\rangle$ adequately represents the bottom stress. A spatially constant c_d often has been used in models (Longuet-Higgins 1970; Thornton and Guza 1986; Özkan-Haller and Kirby 1999). However, within the surf zone c_d is elevated relative to seaward of the surf zone (Feddersen et al. 1998). A drag coefficient proportional to $h^{-1/3}$ (c_d increases in shallower depths) improves 1D $\overline{v}$ model predictions compared with a constant c_d (Ruessink et al. 2001). The elevated surf zone or shallow-water c_d has been hypothesized to result from increased bottom roughness (e.g., Garcez-Faria et al. 1998) or breaking-wave-generated turbulence (e.g., Church and Thornton 1993), but the spatial variation of c_d is not understood.

The wave forcing, c_d, and the Reynolds stress terms are difficult to estimate directly, and therefore the quality of their parameterizations is not known. Instead, parameterizations are accepted or rejected by the accuracy of the model predictions. Parameterizations often can be tuned so that model predictions match a limited dataset and thus, rarely are rejected. Here, an inverse method is developed (section 2) that uses the setup and alongshore current observations and dynamics to solve for parameterized quantities, namely, the cross- and alongshore forcing and the drag coefficient. Specification of the measurement error variances and parameterized forcing and drag coefficient error covariances is required. Inverse solutions not consistent with the specified measurement and parameterization errors are considered spurious and are rejected. The inverse method is tested with a synthetic barred-beach example with known forcing and c_d (section 3), and works well given the number and quality of field observations typically available. The inverse method is applied to one case example each from the Duck94 and SandyDuck field experiments (section 4). The case example inverse results are discussed in the context of wave rollers and possible drag coefficient dependence on breaking-wave-generated turbulence and bed roughness (section 5). The results are summarized in section 6.

2. Inverse modeling

a. Prior model and prior solutions

The equation for the setup (1) is linearized (i.e., the still-water depth h is used instead of $h + \overline{\eta}$) to simplify the inverse problem. Prior model solutions with $\overline{\eta}$ included and excluded in h are similar in water depths $\geq$ 0.3 m, where the case example observations were obtained. The parameterized cross- and alongshore forcings are denoted as the prior forcing $F_x^{(\rm pr)}$ and $F_y^{(\rm pr)}$. The prior drag coefficient $c_d^{(\rm pr)}$ is constant. The offshore ($x = L$) prior boundary condition for the setup model (1) is $\overline{\eta} = 0$. The alongshore current model (2) uses prior slip boundary conditions $d\overline{v}/dx = 0$ at the shoreline ($x = 0$) and offshore ($x = L$) boundaries. The quadratic velocity term in the bottom stress is parameterized with $\langle|\mathbf{u}|v\rangle = B(\overline{v}) = \sigma_T\overline{v}[1.16^2 + (\overline{v}/\sigma_T)^2]^{1/2}$ (Feddersen et al. 2000), where σ_T^2 is the wave-orbital velocity variance. With specified prior forcing, drag coefficient, and boundary conditions, (1) and (2) yield the prior setup $\overline{\eta}^{(\rm pr)}$ and alongshore current $\overline{v}^{(\rm pr)}$.

b. Setup inverse modeling

Error in the setup dynamics $f_x(x)$, attributed to error in the prior wave forcing, is allowed on the right-hand side of the cross-shore momentum equation [(1)]. The inverse forcing is given by $F_x^{(i)} = F_x^{(\rm pr)} - f_x$. The forcing error (or correction) f_x is assumed to be a zero-mean continuous Gaussian random variable with covariance $C_{f_x}(x, x') = E[f_x(x)f_x(x')]$. Similarly, zero-mean Gaussian error with prior variance $\sigma_{\overline{\eta}L}^2$ is allowed in the prior setup boundary condition $\overline{\eta}(L) = 0$. The M noisy $\overline{\eta}$ observations $d_m^{(\overline{\eta})}$ ($m = 1, \ldots, M$) consist of signal and measurement error so that

$$d_m^{(\overline{\eta})} = \overline{\eta}(x_m) + e_m^{(\overline{\eta})},$$

where measurement errors $e_m^{(\overline{\eta})}$ are considered zero-mean identical and independent Gaussian random variables with (prior) variance $\sigma_{\overline{\eta}d}^2$.

Inverse estimates of $\overline{\eta}$ and f_x that incorporate dynamics and data are found by minimizing a cost function that is a combination of dynamical, boundary condition, and data errors (e.g., Bennett 1992):

$$J[\overline{\eta}] = \int\int_0^L f_x(x)C_{f_x}^{-1}(x, x')f_x(x')\,dx'\,dx + \sigma_{\overline{\eta}L}^{-2}\overline{\eta}_L^2 + \sigma_{\overline{\eta}d}^{-2}\sum_{m=1}^{M}[\overline{\eta}(x_m) - d_m^{(\overline{\eta})}]^2, \quad (3)$$

where each component of (3) is weighted by its inverse covariance. The minimum of the cost function yields the inverse setup $\overline{\eta}^{(i)}$ and forcing $F_x^{(i)}$. With each term interpreted as a Gaussian random variable, cost-function minimization corresponds to maximum likelihood estimation (appendix A), and the (statistical) consistency of the inverse solutions with the prior assumptions (i.e., covariances) can be tested (appendix B).

The inverse of $C_{f_x}(x, x')$ is defined so that

$$\int_0^L C_{f_x}(x, x'')C_{f_x}^{-1}(x'', x')\, dx'' = \delta(x - x'), \quad (4)$$

where $\delta(x)$ is the Dirac delta function. The $\overline{\eta}$ adjoint $\lambda_{\overline{\eta}}$ is defined as the convolution of f_x with $C_{f_x}^{-1}$,

$$\lambda_{\overline{\eta}}(x) = \int_0^L C_{f_x}^{-1}(x, x')f_x(x')\, dx', \quad (5)$$

so that

$$f_x(x) = \int_0^L C_{f_x}(x, x')\lambda_{\overline{\eta}}(x')\, dx' = C_{f_x} \cdot \lambda_{\overline{\eta}}.$$

Setting the first variation of the cost function $J[\overline{\eta}]$ to zero yields the Euler–Lagrange equations for the minimum of $J[\overline{\eta}]$:

$$-gh\frac{d\overline{\eta}}{dx} + F_x = C_{f_x} \cdot \lambda_{\overline{\eta}}, \quad (6a)$$

$$(-gh\lambda_{\overline{\eta}} + \sigma_{\overline{\eta}_L}^{-2}\overline{\eta})_{x=L} = 0, \quad (6b)$$

$$g\frac{d(h\lambda_{\overline{\eta}})}{dx} + \sigma_{\overline{\eta}_d}^{-2}\sum_{m=1}^{M}[\overline{\eta}(x_m) - d_m^{(\overline{\eta})}]\delta(x - x_m) = 0, \quad (6c)$$

and

$$\lambda_{\overline{\eta}}|_{x=0} = 0, \quad (6d)$$

which are solved directly for the inverse solutions $\overline{\eta}^{(i)}$ and $f_x^{(i)}$ [or $F_x^{(i)}$].

At the minimum, the cost function $J[\overline{\eta}]$ is rewritten, after integrating by parts, as

$$J[\overline{\eta}^{(i)} + \overline{\eta}'] = J_{\min} + \int\int_0^L \overline{\eta}'[C_{\overline{\eta}}^{(i)}]^{-1}\overline{\eta}'\, dx\, dx', \quad (7)$$

where $J_{\min}$ is the minimum of the cost function (3) found by solving (6), and $\overline{\eta}'$ are deviations from the inverse solution. The curvature of the cost function at the minimum $[C_{\overline{\eta}}^{(i)}(x, x')]^{-1}$ is interpreted as the inverse $\overline{\eta}$ covariance (appendix A). The prior $\overline{\eta}$ covariance $C_{\overline{\eta}}^{(\mathrm{pr})}(x, x')$ is related to the forcing error covariance by removing the data term from $J[\overline{\eta}]$ [(3)] and integrating by parts; that is,

$$[C_{\overline{\eta}}^{(\mathrm{pr})}]^{-1} = g^2\frac{d}{dx}\left\{h(x)\frac{d[h(x')C_{f_x}^{-1}(x, x')]}{dx'}\right\} \quad (8)$$

(neglecting boundary terms). The prior covariance gives the $\overline{\eta}$ uncertainty when no data are available. The inverse $\overline{\eta}$ covariance $C_{\overline{\eta}}^{(i)}(x, x')$ is then given by

$$[C_{\overline{\eta}}^{(i)}]^{-1} = [C_{\overline{\eta}}^{(\mathrm{pr})}]^{-1} + \sigma_{\overline{\eta}_d}^{-2}\sum_{m=1}^{M}\delta(x - x_m)\delta(x' - x_m). \quad (9)$$

The addition of data reduces $C_{\overline{\eta}}^{(i)}$, thus reducing the uncertainty of the inverse solutions.

c. Alongshore current inverse modeling

Analogous to the inverse setup model, error in the alongshore current dynamics $f_y(x)$ is allowed on the right-hand side of (2), and represents error in the forcing, bottom stress, and lateral mixing. Because the forcing is considered to have the largest uncertainty and with the drag coefficient solved for separately, f_y is ascribed to forcing error. Corrections to lateral mixing are neglected. The inverse alongshore wave forcing $F_y^{(i)}$ is given by $F_y^{(i)} = F_y^{(\mathrm{pr})} - f_y$, and the forcing error (or correction) f_y is assumed to be a zero-mean Gaussian random variable with covariance $C_{f_y}(x, x')$. Errors in the prior slip boundary conditions are assumed to be zero-mean Gaussian random variables with variance $\sigma_{\overline{v}_{x0}}^2$ and $\sigma_{\overline{v}_{xL}}^2$ at $x = 0$ and $x = L$. The inverse method also allows for drag coefficient deviations from the prior $c_d^{(\mathrm{pr})}$, adjusting the drag coefficient to make the inverse $\overline{v}$ consistent with the data. The c_d error is considered to be a zero-mean Gaussian random variable with prior covariance $C_{c_d}^{(\mathrm{pr})}(x, x')$. The N noisy alongshore current observations $d_m^{(\overline{v})}$ consist of signal and measurement error, given by

$$d_m^{(\overline{v})} = \overline{v}(x_m) + e_m^{(\overline{v})},$$

where e_m is zero-mean Gaussian measurement error with prior variance $\sigma_{\overline{v}d}^2$.

The cost function $I[\overline{v}, c_d]$ is defined as a combination of dynamical, boundary condition, drag coefficient, and data errors:

$$\begin{aligned} I(\overline{v}, c_d) = {} & \int\int_0^L f_y(x)C_{f_y}^{-1}(x, x')f_y(x')\, dx\, dx' \\ & + \sigma_{\overline{v}_{x0}}^{-2}\left[\frac{d\overline{v}(0)}{dx}\right]^2 + \sigma_{\overline{v}_{xL}}^{-2}\left[\frac{d\overline{v}(L)}{dx}\right]^2 \\ & + \int\int_0^L [c_d(x) - c_d^{(\mathrm{pr})}][C_{c_d}^{(\mathrm{pr})}(x, x')]^{-1} \\ & \qquad \times [c_d(x') - c_d^{(\mathrm{pr})}]\, dx\, dx' \\ & + \sigma_{\overline{v}d}^{-2}\sum_{n=1}^{N}[\overline{v}(x_n) - d_n^{(\overline{v})}]^2, \end{aligned} \quad (10)$$

where each component of the cost function (10) is weighted by its inverse covariance. The minimum of the cost function yields the inverse solutions. With the interpretation of each term as a Gaussian random variable, minimization of the cost function corresponds to

maximum likelihood estimation (appendix A) and allows for testing the consistency of the inverse solution.

Setting the first variation of $I[\overline{v}, c_d]$ with respect to $\overline{v}$ and c_d to zero leads to the Euler–Lagrange equations for the cost function minimum:

$$F_y - c_d B(\overline{v}) + \frac{d}{dx}\left(\nu h \frac{d\overline{v}}{dx}\right) = C_{f_y} \cdot \lambda_{\overline{v}}(x), \quad (11a)$$

$$\left(\frac{d\overline{v}}{dx} - \sigma^2_{\overline{v}_x 0}\, \nu h \lambda_{\overline{v}}\right)_{x=0} = 0, \quad (11b)$$

$$\left(\frac{d\overline{v}}{dx} + \sigma^2_{\overline{v}_x L}\, \nu h \lambda_{\overline{v}}\right)_{x=L} = 0, \quad (11c)$$

$$-c_d \frac{dB}{d\overline{v}} \lambda_{\overline{v}} + \frac{d}{dx}\left(\nu h \frac{d\lambda_{\overline{v}}}{dx}\right) + \sigma^{-2}_{\overline{v}d} \sum_{n=1}^{N} [\overline{v}(x_n) - d_n^{(\overline{v})}]\delta(x - x_n) = 0, \quad (11d)$$

$$\left.\frac{d\lambda_{\overline{v}}}{dx}\right|_{x=0,L} = 0, \quad \text{and} \quad (11e)$$

$$-\lambda_{\overline{v}} B(\overline{v}) + [C_{c_d}^{(\mathrm{pr})}]^{-1} \cdot [c_d - c_d^{(\mathrm{pr})}] = 0, \quad (11f)$$

where the $\overline{v}$ adjoint $\lambda_{\overline{v}}$ is defined similarly to the $\overline{\eta}$ adjoint (5). The set of Euler–Lagrange equations (11) are nonlinear, ordinary differential equations for the inverse solutions $\overline{v}^{(i)}$, $f_y^{(i)}$, and $c_d^{(i)}$.

At the minimum, after linearizing and integrating by parts, the cost function $I[\overline{v}, c_d]$ is rewritten as

$$I[\overline{v}^{(i)} + \overline{v}', c_d^{(i)} + c_d'] = I_{\min} + \int\int_0^L \overline{v}'[C_{\overline{v}}^{(i)}]^{-1}\overline{v}' + c_d'[C_{c_d}^{(i)}]^{-1}c_d' + \overline{v}'[C_{\overline{v},c_d}^{(i)}]^{-1}c_d' + c_d'[C_{c_d,\overline{v}}^{(i)}]^{-1}\overline{v}'\, dx\, dx', \quad (12)$$

where $I_{\min}$ is the minimum of $I[\overline{v}, c_d]$ found by solving (11), and $\overline{v}'$ and c_d' are deviations from the inverse solutions. The curvatures of $I[\overline{v}, c_d]$ at the minimum {e.g., $[C_{\overline{v}}^{(i)}(x, x')]^{-1}$ and $[C_{c_d}^{(i)}]^{-1}$} are interpreted as inverse covariances (appendix A). Similarly, the prior $\overline{v}$ covariance $C_{\overline{v}}^{(\mathrm{pr})}$ is found by taking the first two terms of (10), linearizing about the prior $\overline{v}$ solution, and integrating by parts, resulting in

$$[C_{\overline{v}}^{(\mathrm{pr})}]^{-1} = [c_d^{(\mathrm{pr})}]^2 \frac{dB(x)}{d\overline{v}} \frac{dB(x')}{d\overline{v}} C_{f_y}^{-1}(x, x') - c_d^{(\mathrm{pr})} \frac{dB(x)}{d\overline{v}} \frac{d}{dx'}\left(\nu h \frac{dC_{f_y}^{-1}}{dx'}\right) - c_d^{(\mathrm{pr})} \frac{dB(x')}{d\overline{v}} \frac{d}{dx}\left(\nu h \frac{dC_{f_y}^{-1}}{dx}\right) + \frac{d}{dx}\left\{\nu h \frac{d}{dx}\left[\frac{d}{dx'}\left(\nu h \frac{dC_{f_y}^{-1}}{dx'}\right)\right]\right\} \quad (13)$$

(neglecting boundary terms). The inverse $\overline{v}$ covariance $C_{\overline{v}}^{(i)}$ is given by

$$[C_{\overline{v}}^{(i)}]^{-1} = [C_{\overline{v}}^{(\mathrm{pr})}]^{-1} + \sigma^{-2}_{\overline{v}d} \sum_{n=1}^{N} \delta(x - x_n)\delta(x' - x_n) \quad (14)$$

with $c_d^{(\mathrm{pr})}$ replaced by $c_d^{(i)}$ in $C_{\overline{v}}^{(\mathrm{pr})}$ and $\overline{v}^{(i)}$ used in $dB/d\overline{v}$. As with $\overline{\eta}$, the addition of data reduces the inverse uncertainty. The inverse c_d covariance,

$$[C_{c_d}^{(i)}(x, x')]^{-1} = B(x)C_{f_y}^{-1}(x, x')B(x') + [C_{c_d}^{(\mathrm{pr})}]^{-1}, \quad (15)$$

also is reduced relative to the prior because the first term in (15) is positive definite. The $\overline{v}$–c_d covariance $C_{\overline{v},c_d}$ is not discussed.

d. Prior covariances

Specifying the prior covariances is nontrivial. The covariance form chosen is a homogeneous (i.e., only a function of $x - x'$) bell-shaped covariance often used in objective mapping (e.g., Brethereton et al. 1976):

$$C_\gamma(x, x') = \sigma_\gamma^2 \exp\left[-\frac{(x - x')^2}{l_\gamma^2}\right], \quad (16)$$

where γ is either f_x, f_y, or c_d. The f_x, f_y, and c_d variances ($\sigma_{f_x}^2$, $\sigma_{f_y}^2$, $\sigma_{c_d}^2$) and decorrelation length scales (l_{f_x}, l_{f_y}, and l_{c_d}) must be specified. This covariance form is a significant simplification. In particular, it is unlikely that the true forcing error covariances are homogeneous. Nevertheless, the inverse solutions with (16) appear to work well, as demonstrated below. Nonhomogeneous covariance forms similar to (16), but with (for example) σ_{f_x} proportional to $F_x^{(\mathrm{pr})}$, were implemented. Results were *similar* to those using the homogeneous form (16). The homogeneous form was used for simplicity, because the form of the true covariances is unknown. Note that the homogeneous forcing error covariances, once filtered by the $\overline{\eta}$ and $\overline{v}$ dynamics, result in nonhomogeneous prior and inverse $\overline{\eta}$ [(9)] and $\overline{v}$ [(14)] covariances, and nonhomogeneous inverse c_d [(15)] covariance.

3. Test of the inverse method

The ability of the inverse method to solve for the forcing and drag coefficient is tested with synthetic data. A true cross- and alongshore wave forcing (based on rollers) and a cross-shore variable c_d yield [through (1) and (2)] the true $\overline{\eta}^{(\mathrm{tr})}$ and $\overline{v}^{(\mathrm{tr})}$. Prior (nonroller) forcing and constant c_d similarly yield the prior $\overline{\eta}^{(\mathrm{pr})}$ and $\overline{v}^{(\mathrm{pr})}$ and reflect the imperfect knowledge of the dynamics. The true values represent the dynamical information that the inverse method should reproduce, given the prior values, noisy data, and assumptions about the errors.

a. True and prior conditions

Barred-beach bathymetry h from Duck, North Carolina (Lippmann et al. 1999), is used with a domain

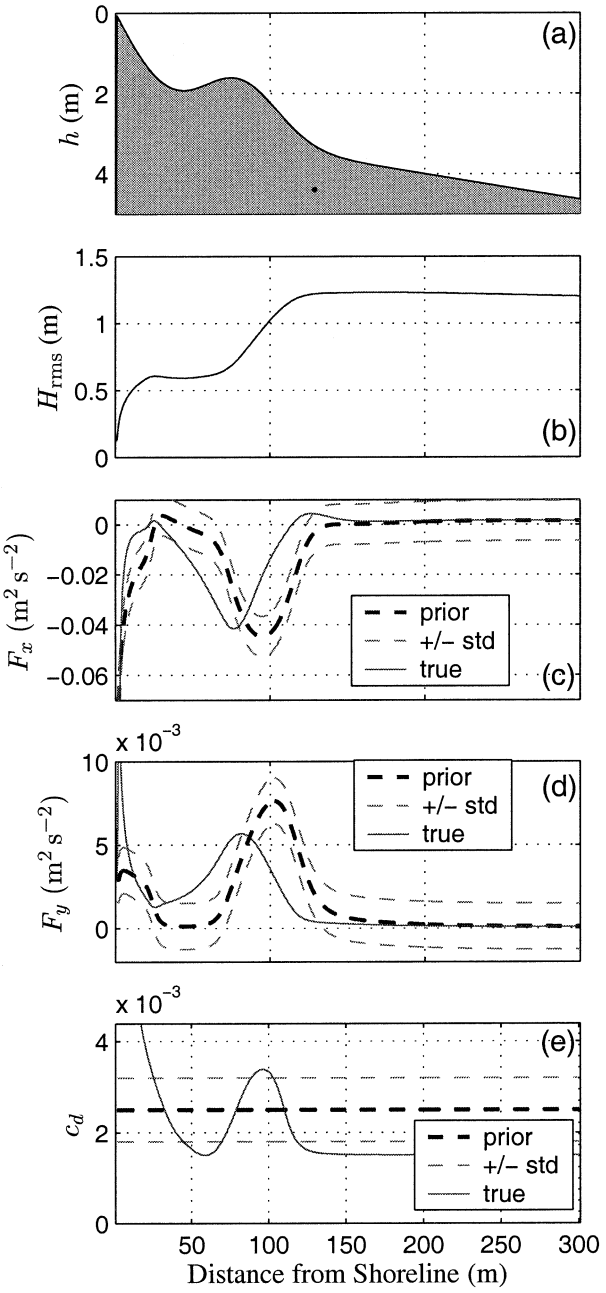

FIG. 1. Test-case conditions vs distance from the shoreline: (a) depth h, (b) wave height H_{rms}, (c) cross-shore forcing F_x, (d) alongshore forcing F_y, and (e) drag coefficient c_d. In (c), (d), and (e), the dark-dashed and light-dashed curves represent the prior and ± 1 std dev, and the solid curves represent the true results.

extending from the shoreline ($x = 0$ m) to 300 m offshore (Fig. 1a). The bar crest is located at $x = 80$ m and has a half-width of 15 m. At the offshore boundary, the wave height $H_{\text{rms}} = 1.2$ m, the wave period is 10 s, and the wave angle is 15° relative to shore-normal. The waves are transformed shoreward (Thornton and Guza 1983) over the barred bathymetry (Fig. 1b), yielding the (without rollers) prior wave forcing $F_x^{(\text{pr})}$ and $F_y^{(\text{pr})}$ (dark dashed curves in Figs. 1c,d), and also the wave-orbital velocity variance σ_T^2. A roller model (Stive and de Vriend 1994; Reniers and Battjes 1997; Ruessink et al. 2001) is used to calculate the true wave forcings $F_x^{(\text{tr})}$ and $F_y^{(\text{tr})}$ (solid curves in Figs. 1c,d). Relative to the prior, the roller model displaces shoreward and reduces the magnitude of the forcing peaks. In addition to the wave forcing, a spatially constant alongshore wind forcing of 10^{-4} m^2 s^{-2} (roughly corresponding to a 14-kt alongshore wind) is added to the prior and true alongshore forcing.

Following Church and Thornton (1993), the true drag coefficient $c_d^{(\text{tr})}$ depends on the wave dissipation with a background (zero wave dissipation) value of 0.0015 (Fig. 1e). Maxima of c_d, just offshore of the bar crest and near the shoreline, occur where breaking-wave dissipation is maximum. This c_d is hypothetical and is used only to test the inverse method. A c_d that depends inversely on water depth [e.g., the Manning–Strickler equation used by Ruessink et al. (2001)] gives qualitatively similar c_d variation. The spatially constant $c_d^{(\text{pr})} = 0.0025$ (Fig. 1e, dashed line) best fits the prior $\overline{v}$ to the data. The spatially constant eddy viscosity $\nu = 0.5$ m^2 s^{-1} was used to model $\overline{v}$ at two different barred beaches (Ruessink et al. 2001) and lies midway within the range of ν (0.1–0.9 m^2 s^{-1}) suggested by Özkan-Haller and Kirby (1999). With this eddy viscosity, the modeled magnitude of lateral mixing is small relative to the forcing (Ruessink et al. 2001).

These inputs are used within the setup [(1)] and alongshore current [(2)] models to generate true and prior $\overline{\eta}$ and $\overline{v}$ (Figs. 2a,b). The sharp increase in the $\overline{\eta}^{(\text{tr})}$ and the main $\overline{v}^{(\text{tr})}$ peak are moved onshore from the prior locations due to the roller and (for $\overline{v}^{(\text{tr})}$) by the reduced $c_d^{(\text{tr})}$ in the bar trough. Differences between the prior and true setup are significant (5 cm) in the bar–trough region. The difference between the prior and true $\overline{v}$ exhibits the classic barred-beach model–data difference when roller models are not included (e.g., Church and Thornton 1993). Noisy $\overline{\eta}$ and $\overline{v}$ data [$d_m^{(\overline{\eta})}$ and $d_m^{(\overline{v})}$, asterisks in Figs. 2a,b] are generated at eight locations by adding to the true values zero-mean Gaussian noise with standard deviations (referred to as std dev) of 0.004 m and 0.05 m s^{-1}, representative of setup measurement (Raubenheimer et al. 2001) and electromagnetic current meter (Feddersen and Guza 2003) error, respectively. The eight data locations are typical of the cross-shore instrumented transects at Duck during the Duck Experiment on Low-Frequency and Incident-Band Longshore and Across-Shore Hydrodynamics (DELILAH), Duck94, and SandyDuck field experiments.

b. Prior covariances

The prior covariances of the forcing, drag coefficient, boundary condition, and data errors also must be specified. The data errors $\sigma_{\overline{\eta}d} = 0.004$ m and $\sigma_{\overline{v}d} = 0.05$ m s^{-1} are those used to create the synthetic data. The

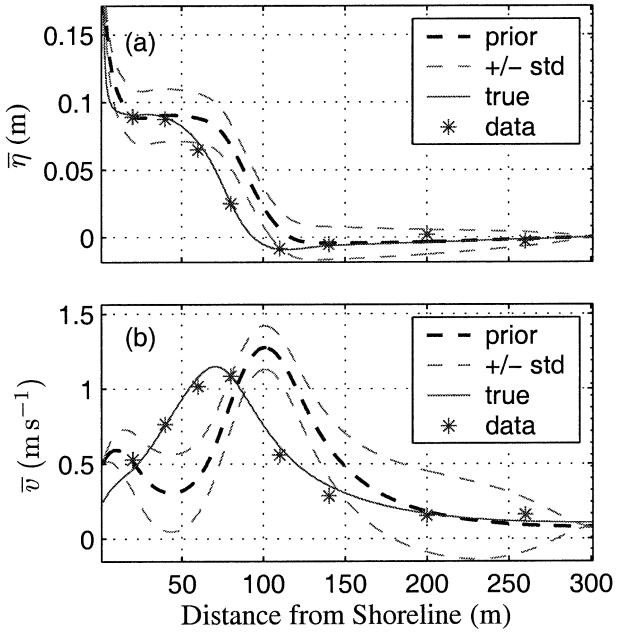

FIG. 2. Prior and true (a) setup $\overline{\eta}$ and (b) alongshore current $\overline{v}$ vs distance from the shoreline. The dark- and light-dashed curves represent the prior and ± 1 std dev. The solid curves represent the true results. The asterisks represent the (noisy) data.

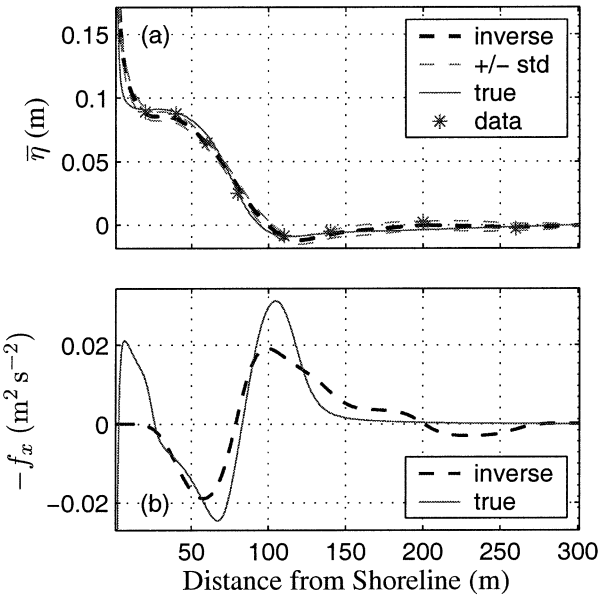

FIG. 3. (a) Inverse (dashed), true (solid), and data (asterisks) $\overline{\eta}$, and (b) inverse (dashed) and true (solid) cross-shore forcing correction f_x vs distance from the shoreline. In (a), the dark- and light-dashed curves represent the inverse and ± 1 std dev.

magnitude of the forcing error is constrained by the prior forcing magnitude. Because the prior forcing is believed to be qualitatively correct, the forcing errors σ_{f_x} and σ_{f_y} are chosen to be 18% of the bar crest prior $|F_x^{(\mathrm{pr})}|$ and $|F_y^{(\mathrm{pr})}|$ maxima. The prior forcing ± 2 std dev (σ_{f_x} and σ_{f_y}) are consistent with the true forcing (light dashed curves in Figs. 1c,d); however, this consistency cannot be examined in general with unknown true forcing. The c_d error $\sigma_{c_d} = 0.0007$ is chosen such that the $c_d^{(\mathrm{pr})} \pm 2\sigma_{c_d}$ spans the expected c_d range (0.001–0.004). The prior $c_d^{(\mathrm{pr})} \pm 2\sigma_{c_d}$ also mostly contains the true c_d (Fig. 1e). Because the bathymetry strongly controls the wave properties, the forcing and c_d error length scales are chosen to match the sandbar half-width ($l_{f_x} = l_{f_y} = l_{c_d} = 15$ m). Varying the length scales between 10 and 30 m does not change the inverse solutions significantly in this or subsequent sections. The $\overline{\eta}$ offshore boundary condition error $\sigma_{\overline{\eta}L} = 0.01$ m. The $\overline{v}$ boundary condition errors are $\sigma_{\overline{v}_x 0} = 0.05$ s^{-1} and $\sigma_{\overline{v}_x L} = 0.01$ s^{-1}, allowing for typical boundary shear of 1 m s^{-1} over 20 m at $x = 0$ m and 0.2 m s^{-1} over 20 m at $x = L$. The prior $\overline{\eta}$ and $\overline{v}$ boundary condition errors do not affect the inverse solutions significantly. The prior covariances $C_{\overline{\eta}}^{(\mathrm{pr})}$ [(8)] and $C_{\overline{v}}^{(\mathrm{pr})}$ [(13)] are estimated using the forcing covariances (light-dashed curves in Figs. 2a,b). One measure of consistency in the forcing error covariances is that most of the $\overline{\eta}$ and $\overline{v}$ data are within two std dev (defined as the square root of the covariance diagonal) of the prior $\overline{\eta}$ and $\overline{v}$. This test can be applied in real inverse situations.

c. Inverse solution

With all the ingredients, the inverse method yields the inverse setup $\overline{\eta}^{(i)}$ (Fig. 3a), inverse alongshore current $\overline{v}^{(i)}$ (Fig. 4a), and their covariances $C_{\overline{\eta}}^{(i)}$ [(9)] and $C_{\overline{v}}^{(i)}$ [(14)]. The inverse solutions agree well with the true $\overline{\eta}^{(\mathrm{tr})}$ and $\overline{v}^{(\mathrm{tr})}$ and are significant improvements over the prior solutions (Figs. 2a,b). The rms differences between inverse solutions and data are 2.4 mm and 2.6 cm s^{-1} for $\overline{\eta}$ and $\overline{v}$, respectively, consistent (at the 95% level) with the prior data error variance (appendix B). Inverse solutions should pass this test if they are to be accepted. The addition of data significantly reduces the uncertainty in the inverse solutions (the inverse $\overline{\eta}$ and $\overline{v}$ std dev are 20%–50% of the prior). Note that the inverse solutions ± 2 std dev usually contain the true solutions and the data. In regions with instrument gaps much larger than the 15-m decorrelation length scale ($140 < x < 200$ m), the inverse uncertainty increases.

The ability of the inverse method to reproduce the cross- and alongshore forcing is examined by comparing the inverse forcing corrections [$f_x^{(i)}$ and $f_y^{(i)}$] with the true forcing corrections $f_x^{(\mathrm{tr})}$ [i.e., $F_x^{(\mathrm{tr})} - F_x^{(\mathrm{pr})}$] and $f_y^{(\mathrm{tr})}$ (Figs. 3b and 4b). The inverse $f_x^{(i)}$ and $f_y^{(i)}$ qualitatively reproduce $f_x^{(\mathrm{tr})}$ and $f_y^{(\mathrm{tr})}$, and result in significant improvements over the prior forcings. The location and magnitude of the forcing correction peaks are similar, although $f_x^{(\mathrm{tr})}$ is underpredicted around $x = 110$ m. Onshore of the last data point ($x = 20$ m), without information (data) for the inverse, $f_x^{(i)}$ and $f_y^{(i)}$ relax to zero. The cross- and alongshore inverse forcing corrections are consistent with their prior covariances (appendix B). The $c_d^{(i)}$ is consistent with the prior c_d covariance and

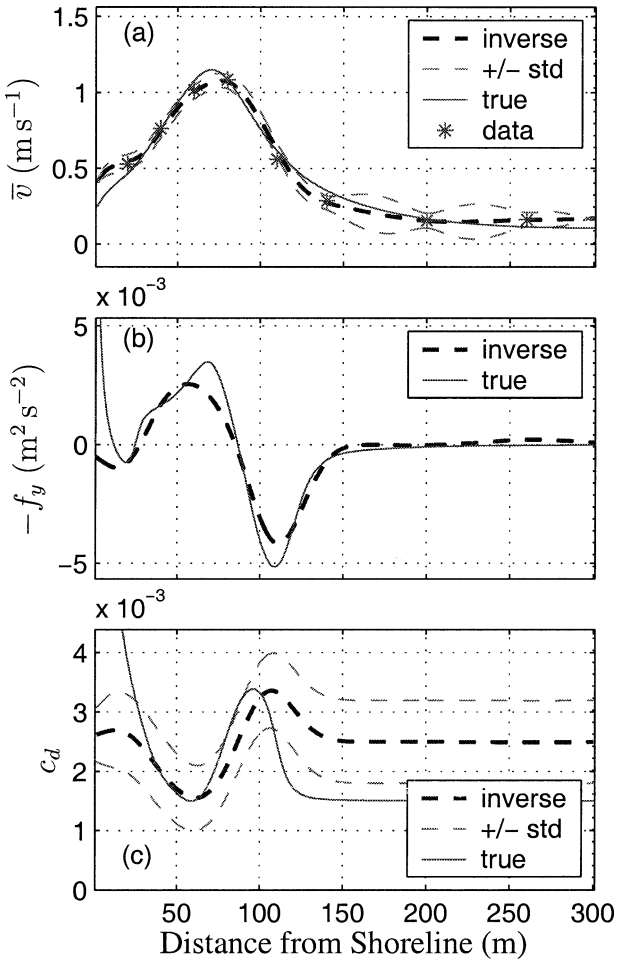

FIG. 4. (a) Inverse (dashed), true (solid), and data (asterisks) $\overline{v}$; (b) inverse (dashed) and true (solid) alongshore forcing correction f_y; and (c) inverse (dashed) and true (solid) c_d vs distance from the shoreline. In (a) and (c), the dark- and light-dashed curves represent the inverse and ± 1 std dev.

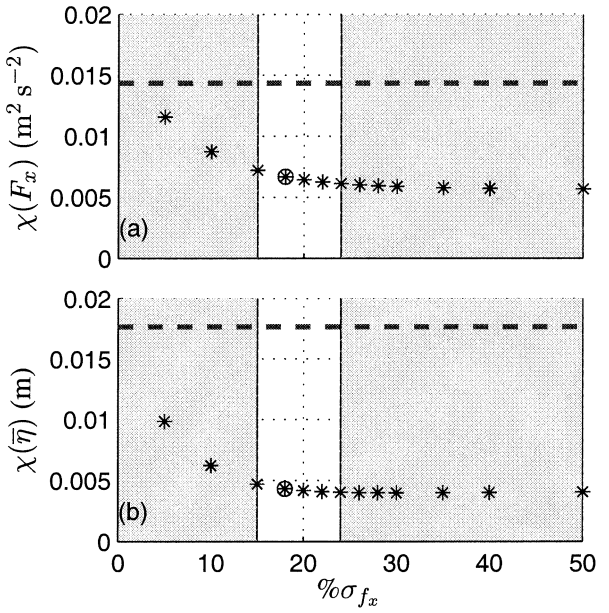

FIG. 5. Misfits [(17)] vs $\%\sigma_{f_x}$ (% of maximum prior forcing magnitude): (a) inverse (asterisks) and prior (dashed line) cross-shore forcing misfit $\chi(F_x)$, and (b) inverse (asterisks) and prior (dashed line) setup misfits $\chi(\overline{\eta})$. The shaded areas are regions where either the data fit (right region) or $f_x^{(i)}$ (left region) is inconsistent with the prior covariances. The circled asterisk indicates the solution in Fig. 3.

qualitatively reproduces $c_d^{(\mathrm{tr})}$ in the bar crest–trough region where the data are concentrated (Fig. 4c). Onshore of $x = 20$ m and offshore of $x = 150$ m, the $c_d^{(i)}$ relaxes back to the prior $c_d = 0.0015$ both because of the data sparseness and because the inverse method can adjust f_y to match the data with less cost. In the bar-trough region, the $c_d^{(i)}$ uncertainties are reduced 15%–30% relative to the prior (Fig. 4c), which is less than the reduction in the $\overline{\eta}$ and $\overline{v}$ uncertainties. These results suggest that the inverse method is capable of solving for the unknown surf-zone cross-shore forcing, alongshore forcing, and drag coefficient given the number and quality of data typically available.

d. Choosing covariance parameters

With the chosen covariance parameters, the inverse solutions pass the consistency tests and reproduce the true solutions. However, with real observations the choice of prior covariances is important and not straightforward. The effect of varying covariance parameters on the inverse solutions is examined to provide guidelines for general application. The boundary condition variances, data variances, and covariance length scales are held fixed at values used previously while σ_{f_x}, σ_{f_y}, and σ_{c_d} are varied. The misfit between the true and inverse solutions is characterized by the metric

$$\chi[\alpha^{(i)}] = \sqrt{\frac{1}{L}\int_{x=20\ \mathrm{m}}^{x=200\ \mathrm{m}} [\alpha^{(i)} - \alpha^{(\mathrm{tr})}]^2\, dx}. \qquad (17)$$

The integral spans the bar-crest region ($x = 20$–200 m) where data are concentrated, L is the integration distance (180 m), and α is any inverse or prior solution [e.g., $F_x^{(i)}$].

For the $\overline{\eta}$ inverse, σ_{f_x} is varied between ($\%\sigma_{f_x}$) 5% and 50% of the bar-crest prior $|F_x^{(\mathrm{pr})}|$ maximum (18% was used in Fig. 3). The $F_x^{(i)}$ and $\overline{\eta}^{(i)}$ misfits are reduced with increasing σ_{f_x} (Fig. 5), and for $\%\sigma_{f_x} > 10\%$, the $F_x^{(i)}$ and $\overline{\eta}^{(i)}$ misfits are 33%–50% and 25%–33% (respectively) of their prior misfits. The largest $\%\sigma_{f_x}$ result in the smallest misfit. However, the inverse solutions with $\%\sigma_{f_x} > 24\%$ (right-hand shaded area in Fig. 5) are inconsistent because of data overfit (inverse solution matches data more closely than warranted, given the observational error), and solutions with $\%\sigma_{f_x} < 16\%$ (left-hand shaded area in Fig. 5) result in $f_x^{(i)}$ being inconsistent with the prior C_{f_x}. Inconsistent solutions are rejected. For the consistent solutions (16% $\leq$

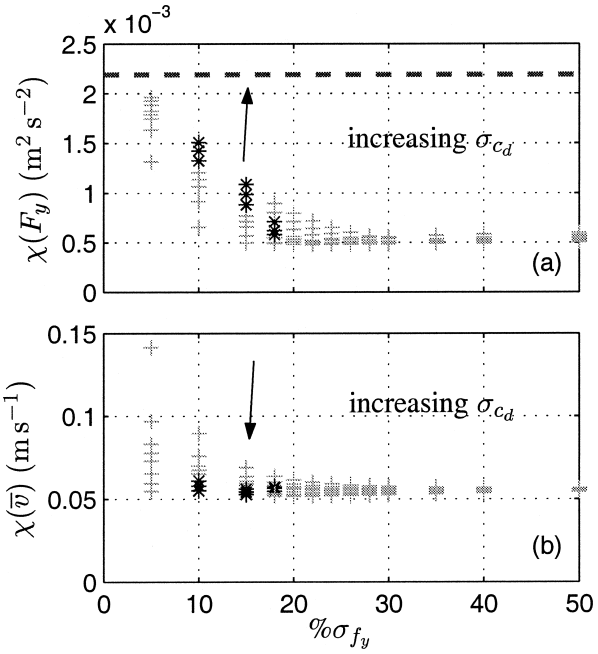

FIG. 6. Misfits [(17)] for (a) inverse alongshore forcing $\chi[F_y^{(i)}]$ and (b) inverse alongshore current $\chi[\overline{v}^{(i)}]$ vs $\%\sigma_{f_y}$. The asterisks represent consistent inverse solutions. The pluses represent inconsistent inverse solutions. The horizontal dashed curve in (a) represents the prior forcing uncertainty $\chi[F_y^{(pr)}] = 0.0022$ m^2 s^{-2}. The prior alongshore current misfit $\chi[\overline{v}^{(pr)}] = 0.40$ m s^{-1} is not shown in (b).

$\%\sigma_{f_x} \leq 24\%$), the $F_x^{(i)}$ and $\overline{\eta}^{(i)}$ misfits are small, near the minimum misfits for all $\%\sigma_{f_x}$. Within the $\%\sigma_{f_x}$ window of consistent solutions, larger $\%\sigma_{f_x}$ are the most accurate. The $f_x^{(i)}$ of the consistent solutions are almost identical.

For the $\overline{v}$ inverse, σ_{f_y} is varied between 5% and 50% ($\%\sigma_{f_y}$) of the maximum bar crest $F_y^{(pr)}$ and σ_{c_d} is varied between 10% and 45% of the constant $c_d^{(pr)}$. The inverse results in improved $F_y^{(i)}$ with misfit 68% to 23% of the $F_y^{(pr)}$ misfit, depending on σ_{c_d} (Fig. 6a). For fixed $\%\sigma_{f_y}$, an increased σ_{c_d} results in a larger $F_y^{(i)}$ misfit (denoted by the arrow in Fig. 6a) because the inverse adjusts $c_d^{(i)}$ instead of the forcing to fit the data. With adjustment of both the forcing and c_d error, the $\overline{v}^{(i)}$ misfit reduction is dramatic {$\chi[\overline{v}^{(i)}]$ is 20% of the $\overline{v}^{(pr)}$ misfit}. The $c_d^{(i)}$ misfit $\chi[c_d^{(i)}]$ (not shown) is reduced only about 15% of the prior $\chi[c_d^{(pr)}]$ because of the cross-shore lag between $c_d^{(i)}$ and $c_d^{(tr)}$ maxima (Fig. 4c). As with the $\overline{\eta}$ inverse, the largest values of $\%\sigma_{f_y}$ have the smallest misfits, but fail at least one consistency test (pluses in Fig. 6). The inverse solutions (asterisks in Fig. 6) that pass all consistency tests have small $\chi[\overline{v}^{(i)}]$. Consistent solutions with larger $\%\sigma_{f_y}$ and σ_{c_d} have small $F_y^{(i)}$ misfit. Within the $\%\sigma_{f_y}$ and σ_{c_d} window of consistent solutions, larger values of these parameters are best. All consistent $f_y^{(i)}$ and $c_d^{(i)}$ solutions exhibit the pattern shown in Fig. 4, only with varying amplitude (factor of 2) depending on $\%\sigma_{f_y}$ and σ_{c_d}.

4. Case examples

The inverse method is applied to observations from two field experiments at Duck: Duck94 (Elgar et al. 1997; Feddersen et al. 1998; Ruessink et al. 2001) and SandyDuck (Elgar et al. 2001; Raubenheimer et al. 2001; Feddersen and Guza 2003; Noyes et al. 2004). Bathymetries are smoothed with a 10-m cutoff wavelength to remove bedforms that dominate the variance in the 1–5-m wavelength band (Thornton et al. 1998). All wave, setup, and alongshore current observations are based on hourly averages. In both cases the bathymetry is alongshore uniform, and the mean alongshore currents are consistent with 1D dynamics (Feddersen et al. 1998; Ruessink et al. 2001; Feddersen and Guza 2003).

a. Duck94 example

During Duck94, there were no setup observations, so only the alongshore current inverse method is applied. Wave breaking occurs offshore of and on the crest ($x = 110$ m) of a well-developed sandbar (Figs. 7a,b). In the bar trough (40–80 m from the shoreline), the wave height remains constant. A tuned 1D wave model (without rollers) (e.g., Thornton and Guza 1983) accurately (rms error 2.2 cm) predicts the wave height evolution (solid curve in Fig. 7b). The wave model (initialized with offshore $H_{\rm rms}$ and S_{xy} estimated from an array of pressure sensors in 8-m water depth), together with $\tau_y^{\rm wind}$ observations, gives the prior $F_y^{(pr)}$ (Fig. 7c). The constant $c_d^{(pr)} = 0.0015$, based on alongshore momentum balances (Feddersen et al. 1998), results in similar data and prior $\overline{v}^{(pr)}$ peak magnitudes (Fig. 7d). The prior $\%\sigma_{f_y}$ is 20% (light dashed curves in Fig. 7c), slightly larger than the largest test-case $\%\sigma_{f_y}$ yielding consistent solutions (section 3d). The $\sigma_{c_d} = 4.5 \times 10^{-4}$, 30% of the prior $c_d^{(pr)}$. The length scales (l_{f_y} and l_{c_d}) are 20 m, approximately the bar half-width. The eddy viscosity $\nu = 0.5$ m^2 s^{-1} is that used by Ruessink et al. (2001) to model a larger dataset from which one of the case examples is drawn. Inverse solutions with ν ranging between 0.1 and 2 m^2 s^{-1} were similar, with smoother inverse solutions for larger ν (not shown). For these ν, the magnitude of the lateral mixing term was small and did not qualitatively change the results. The prior $F_y^{(pr)}$ and $c_d^{(pr)}$ (and prior covariances) are used to calculate $\overline{v}^{(pr)}$ and its error bars (Fig. 7d). Typical of barred-beach $\overline{v}$ model runs without rollers, the prior $\overline{v}^{(pr)}$ rms errors (0.28 m s^{-1}) are substantial.

The $\overline{v}$ inverse method (section 2b), applied with data uncertainty $\sigma_{\overline{v}d} = 0.05$ m s^{-1}, yields solutions (Fig. 8) that pass the consistency tests and agree well with the $\overline{v}$ data (rms error of 0.038 m s^{-1}). The $\overline{v}$ uncertainty is reduced significantly. The $F_y^{(i)}$ is reduced offshore of and on the bar crest ($x \geq 110$ m), and is increased toward the trough ($60 < x < 90$ m), consistent with the concept of a wave roller (Fig. 8b). The slightly negative $F_y^{(i)}$

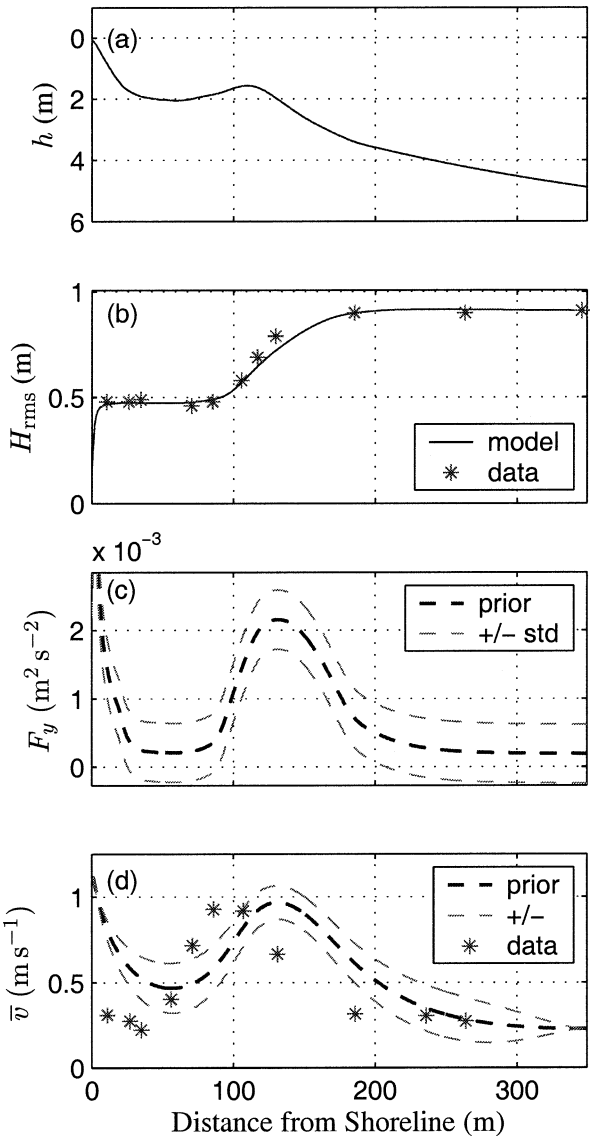

FIG. 7. Duck94 conditions (1700 EST 10 Oct 1994) vs distance from the shoreline: (a) depth h, (b) model (solid) and data (asterisks) wave height H_{rms}, (c) $F_y^{(\text{pr})}$, and (d) prior (dashed) and data (asterisks) $\overline{v}$. In (c) and (d), the dark- and light-dashed curves represent the prior and ± 1 std dev.

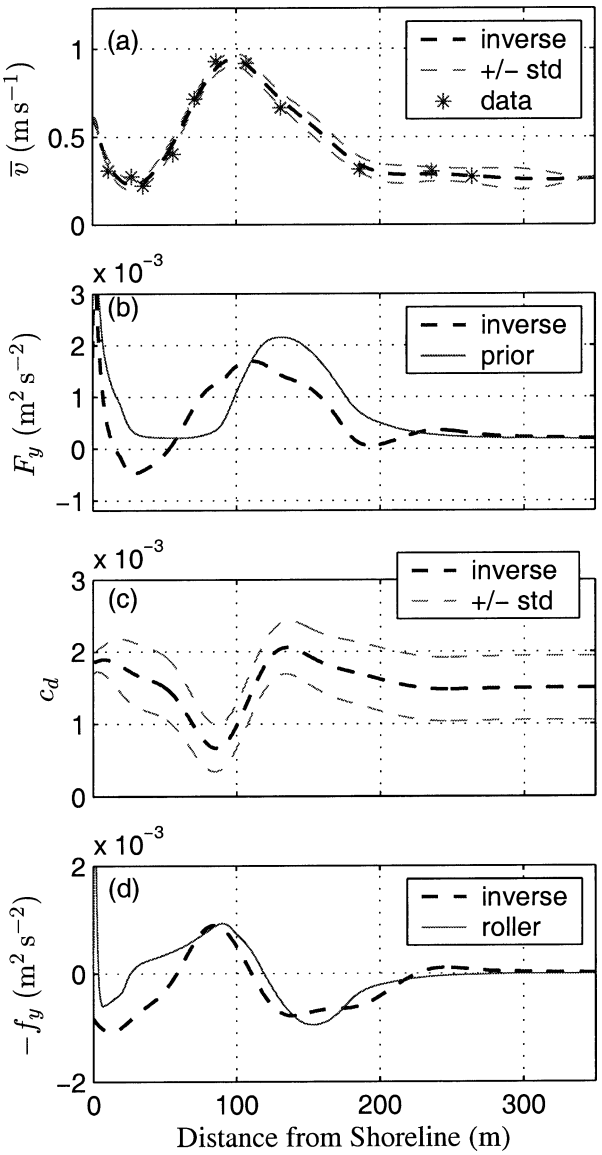

FIG. 8. Duck94 inverse solutions vs distance from the shoreline: (a) inverse (dashed) and data (asterisks) $\overline{v}$, (b) inverse (dashed) and prior (solid) F_y, (c) inverse c_d, and (d) inverse (dashed) and roller (solid) f_y. In (a) and (c), the dark- and light-dashed curves represent the inverse solution and ± 1 std dev. The roller forcing correction $f_y^{(r)}$ in (d) uses roller parameter $\beta = 0.05$ (Ruessink et al. 2001).

near $x = 30$ m indicates a reversal of forcing and, although consistent with the f_y error covariance, seems physically unrealistic (no mechanism for reversal is known). This may be the result of data noise mapped into the forcing correction. The $c_d^{(i)}$ increases just offshore of the bar crest and is reduced in the trough (Fig. 8c). The $c_d^{(i)}$ error bars are reduced by 15%–25% relative to the prior in the crest–trough region where data are concentrated. The inverse forcing correction $f_y^{(i)}$ is compared with the change in alongshore forcing $[f_y^{(r)}]$ calculated from a roller model (Stive and de Vriend 1994; Reniers and Battjes 1997). The inverse and roller reduction in alongshore forcing on and offshore of the bar crest ($110 \leq x < 200$ m) are quite similar (Fig. 8d), as is the increase in alongshore forcing in much of the bar trough ($70 < x < 100$ m). Within the $\%\sigma_{f_y}$ and σ_{c_d} window for consistent inverse solutions, the $f_y^{(i)}$ and $c_d^{(i)}$ have the same structure as in Figs. 8b and 8c but with amplitude varying by 33% and 25%, respectively.

b. SandyDuck example

The SandyDuck case example does not have a well-developed bar (Fig. 9a). There is a steep slope region for $25 < x < 100$ m and a nearly constant depth terrace

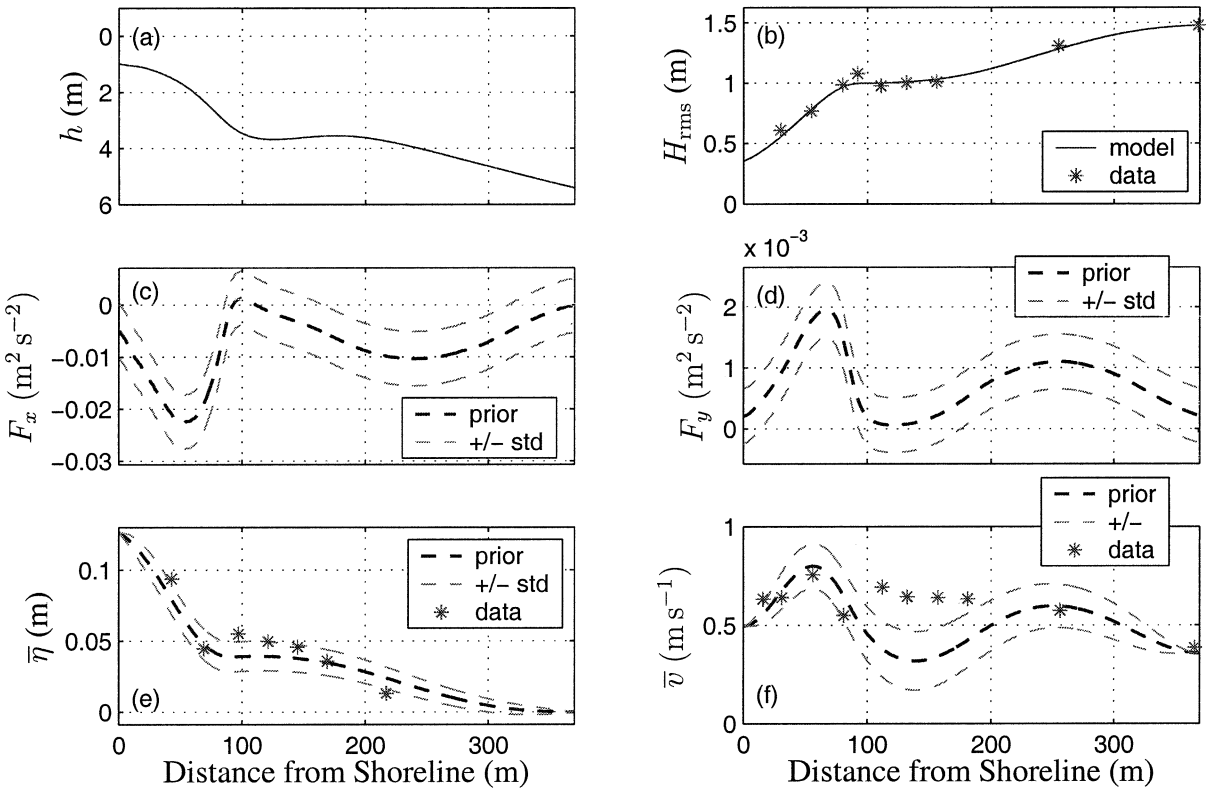

FIG. 9. SandyDuck conditions (1600 EST 18 Oct 1997) vs distance from the shoreline: (a) depth h, (b) model (solid) and data (asterisks) wave height H_{rms}, (c) prior cross-shore forcing $F_x^{(pr)}$, (d) prior alongshore forcing $F_y^{(pr)}$, (e) prior (dashed) and data (asterisks) $\overline{\eta}$, and (f) prior (dashed) and data (asterisks) $\overline{v}$. In (c)–(f), the dark- and light-dashed curves represent the prior and ± 1 std dev.

for $100 < x < 200$ m. Large waves begin breaking offshore of the terrace, have approximately constant height over the terrace, and then dissipate rapidly farther onshore on the steep slope (asterisks in Fig. 9b). A tuned 1D wave model (without rollers) accurately (rms error of 4 cm) predicts the wave height evolution (Fig. 9b). The wave model and observed wind give the prior $F_x^{(pr)}$ and $F_y^{(pr)}$ (Figs. 9c,d). The prior $c_d^{(pr)} = 0.0015$ (not shown). The σ_{f_x} and σ_{f_y} are chosen as 23% of the $F_x^{(pr)}$ and $F_y^{(pr)}$ absolute maxima (light dashed curves in Figs. 9c,d), and $\sigma_{c_d} = 7 \times 10^{-4}$. Large covariance parameters within the window of parameters giving consistent solutions are chosen (section 3d). Although there is no sandbar to set the length scales, l_{f_x}, l_{f_y}, and l_{c_d} are set at 20 m (the same as in Duck94), which is a length scale for significant depth or wave height variation. The eddy viscosity from the Duck94 case example is used. The prior values and covariances are used to calculate $\overline{\eta}^{(pr)}$ and $\overline{v}^{(pr)}$ with error bars (Figs. 9e,f). The errors in the (nonroller) prior model predictions of setup (rms error of 1 cm) and the alongshore current (rms error of 0.2 m s^{-1}) exceed those expected from instrument noise alone. The expected $\overline{\eta}$ data error ($\sigma_{\overline{\eta}d} = 0.003$ m) is based on rms errors of setdown predictions (Raubenheimer et al. 2001), and $\sigma_{\overline{v}d} = 0.05$ m s^{-1}.

Consistent inverse solutions for $\overline{\eta}^{(i)}$ and $\overline{v}^{(i)}$ (Figs. 10a and 11a) agree well with the data (rms errors of 3.9 mm and 3.3 cm s^{-1}, respectively) with significantly reduced uncertainties. Both the cross- and alongshore inverse forcing magnitudes are increased relative to the prior in the terrace region ($100 < x < 200$ m) and are reduced near $x = 80$ m (Figs. 10b and 11b). As with the Duck94 example, changes in the cross- and alongshore forcing are consistent with the roller concept. The inverse model makes $F_x^{(i)}$ slightly positive, predicting setdown for $85 < x < 100$ m to match the setup observations in this region, consistent with observed wave shoaling at $x = 100$ m (Fig. 9b). The $c_d^{(i)}$ pattern (Fig. 11c) is similar to the Duck94 case example (Fig. 8c). In the terrace region, $c_d^{(i)}$ is reduced relative to the prior and is increased on the steep slope region for $70 < x < 90$ m (Fig. 9b). The $c_d^{(i)}$ error bars are reduced 25%–30% where data are concentrated. The cross- and alongshore inverse forcing corrections [$f_x^{(r)}$ and $f_y^{(r)}$] are compared with the change in forcing predicted by the same roller model used in the Duck94 case example. The $f_x^{(i)}$ and $f_x^{(r)}$ qualitatively agree for $50 < x < 250$ m (Fig. 10c). Offshore of $x = 250$ m, where there are no data, $f_x^{(i)}$ is near zero, whereas nonzero $f_x^{(r)}$ is predicted. The $f_y^{(i)}$ and $f_y^{(r)}$ also qualitatively agree for $50 < x < 200$ m, although there is a factor of 2 difference in the magnitude of the $f_y^{(i)}$ and $f_y^{(r)}$ minima at $x = 80$ m (Fig. 11d).

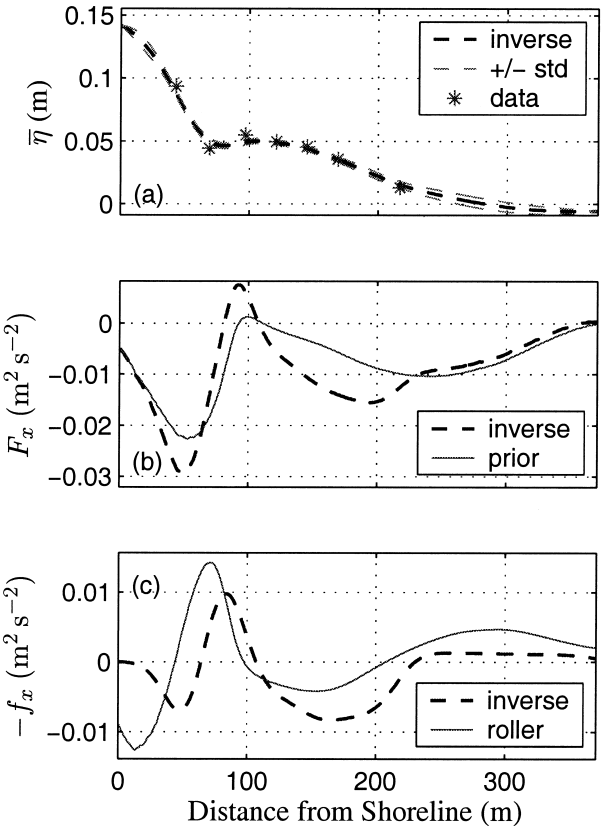

FIG. 10. SandyDuck $\overline{\eta}$ inverse solutions vs distance from the shoreline: (a) inverse (dashed) and data (asterisks) setup $\overline{\eta}$, (b) inverse (dashed) and prior (solid) F_x, and (c) inverse (dashed) and roller (solid) cross-shore forcing corrections f_x. In (a) and (c), the dark- and light-dashed curves represent the inverse solution and ± 1 std dev.

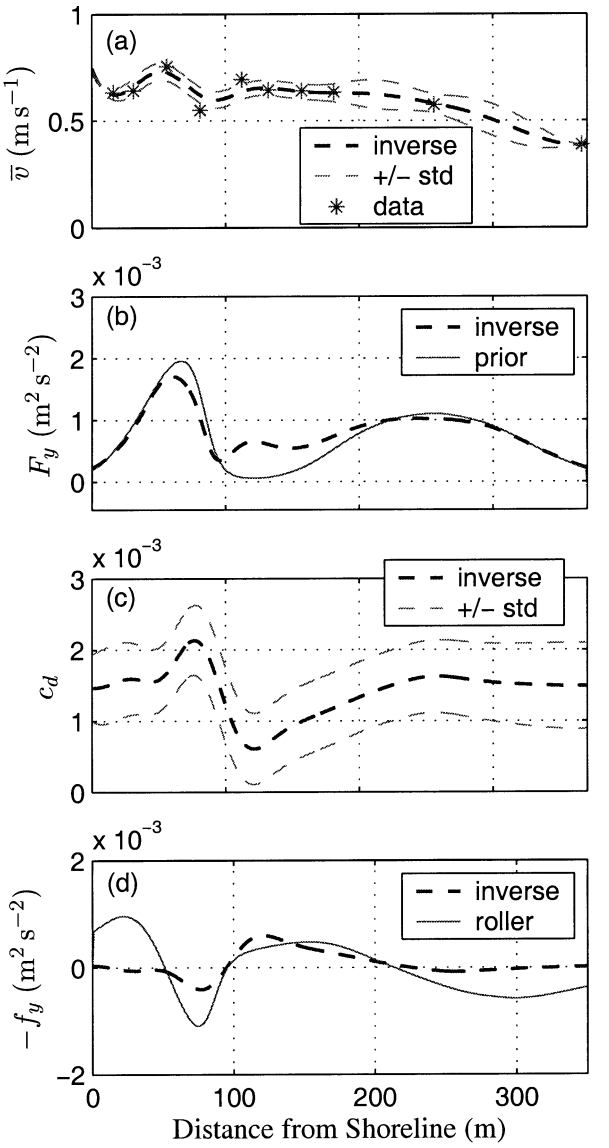

FIG. 11. SandyDuck $\overline{v}$ inverse vs distance from the shoreline: (a) inverse (dashed) and data (asterisks) $\overline{v}$, (b) inverse (dashed) and prior (solid) F_y, (c) inverse (dashed) c_d, and (d) inverse (dashed) and roller (solid) alongshore forcing correction f_y. In (a) and (c), the dark- and light-dashed curves represent the inverse solution and ± 1 std dev.

5. Discussion

Overall, agreement between both the Duck94 and SandyDuck inverse forcing corrections and the roller model is remarkable, particularly because $f_x^{(i)}$ and $f_y^{(i)}$ are independent. No tuning of either the roller model parameters or of the forcing or drag coefficient error covariances was made to maximize this agreement. While the inverse forcings tantalizingly suggest that the roller model accurately predicts the change in cross- and alongshore forcing, no endorsement of a particular roller model is intended here. Varying the covariance parameters by 25% does not change the inverse case example results significantly, although not all inverse solutions are consistent with the prior assumptions.

Inferences can be drawn from the inverse-derived c_d. Assuming that the maximum (and minimum) $c_d^{(i)}$ is a Gaussian random variable with variance given by its zero-lag inverse covariance, the probability that the maximum (and minimum) c_d is increased (reduced) from the prior c_d can be calculated to determine the statistical significance of $c_d^{(i)}$ variation. From both the Duck94 and SandyDuck case examples (Figs. 8c and 11c), the probability is over 90% that the maximum (and minimum) c_d is significantly increased (reduced) from the prior.

Hypotheses that c_d depends either on the bed roughness k_{rms} (e.g., Garcez-Faria et al. 1998) or on breaking-wave-generated turbulence (e.g., Church and Thornton 1993) are examined. Wave dissipation, a measure of the breaking-wave-generated turbulence source, is calculated from the modeled wave energy flux gradients in the region where $c_d^{(i)}$ differs from the prior c_d. A relationship between wave dissipation and $c_d^{(i)}$ is observed (Fig. 12a) in both case examples (correlations $r = 0.64$ and $r = 0.90$ for Duck94 and SandyDuck, respectively), which is consistent with the hypothesis that increases

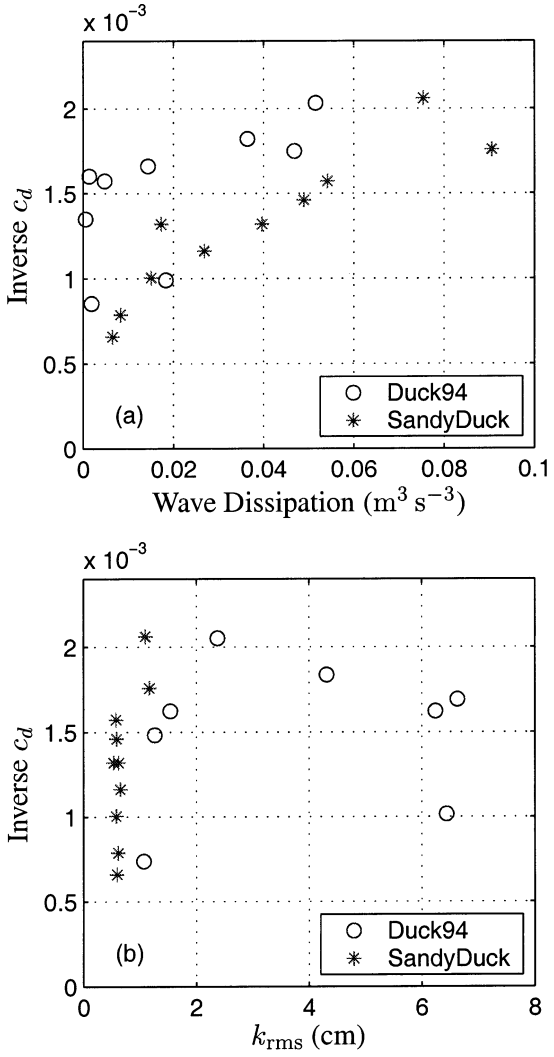

FIG. 12. (a) Duck94 (circles) and SandyDuck (asterisks) inverse c_d vs modeled wave dissipation (Figs. 7b and 9b). Comparison is made for $50 < x < 250$ m (Duck94) and $30 < x < 200$ m (SandyDuck) averaged over the decorrelation length scale $l_{c_d} = 20$ m, yielding approximately independent c_d estimates. Changing the comparison regions does not alter the results. (b) Duck94 (open circles) and SandyDuck (small filled circles) $c_d^{(i)}$ vs bed roughness k_{rms}. The SandyDuck results span $35 < x < 250$ m and are averaged over $l_{c_d} = 20$ m.

in wave dissipation result in increased c_d. No explicit or implicit connection exists in the inverse method between c_d and wave dissipation. Bed roughness k_{rms} was estimated with eight fixed altimeters (Duck94) (Feddersen et al. 2003) and a towed altimeter (SandyDuck) (Gallagher et al. 2003). For the Duck94 example, k_{rms} varies between 1 and 7 cm, but for the SandyDuck example, the bed was smooth ($k_{rms} < 2$ cm). No relationship (i.e., statistically significant correlation) between k_{rms} and $c_d^{(i)}$ exists for either the Duck94 or SandyDuck case, nor does a relationship exist between k_{rms}/h and $c_d^{(i)}$ (not shown). Although the fixed-altimeter-based k_{rms} have errors (Feddersen et al. 2003), the lack of a relationship suggests that bed roughness is not a primary factor in determining c_d (e.g., Feddersen et al. 2003).

The two inverse realizations presented here are insufficient to draw conclusions regarding forcing or c_d parameterizations. Many inverse realizations of the forcing correction and c_d, spanning a wide range of conditions, would allow statistical testing of wave-forcing or c_d hypotheses. Additional interpretations of the inverse solutions are possible. For example, the alongshore forcing error could be ascribed to tidal (e.g., Ruessink et al. 2001) or buoyancy (e.g., Lentz et al. 2003) forcing.

6. Summary

Uncertainties regarding wave-forcing and drag coefficient parameterizations in the nearshore have motivated development of an inverse method that combines dynamics and data to yield optimal estimates of the setup $\overline{\eta}$ and alongshore current $\overline{v}$, together with corrections to the cross-shore forcing, alongshore forcing, and the drag coefficient c_d. The method also yields error bars (covariances) for the $\overline{\eta}$, $\overline{v}$, and c_d inverse solutions. Tests that determine the consistency of the inverse solutions with prior assumptions were presented. The inverse method was tested with a synthetic barred-beach example, and consistent inverse solutions reproduced well the specified true cross- and alongshore forcing and c_d.

The method was applied to two case examples from field experiments yielding inverse solutions that passed the consistency tests. The independently estimated cross- and alongshore inverse forcing corrections were similar to the modeled effect of wave rollers. The significant cross-shore variation of the inverse-derived c_d was related to variations in wave dissipation, but was not related to variation in the observed bed roughness. Although consistent with the hypothesis that breaking-wave-generated turbulence increases c_d, the two examples are not sufficient to examine this relationship statistically. Additional field cases spanning a wide range of nearshore conditions are needed to test hypotheses about the wave forcing and drag coefficient.

Acknowledgments. This research was supported by ONR, NSF, NOPP, and WHOI. The Duck94 and SandyDuck instruments were constructed, deployed, and maintained by staff from the Integrative Oceanography Division of SIO. Britt Raubenheimer helped design and manage the SandyDuck field experiment and provided high-quality setup data. Tom Herbers provided wave observations, and Edie Gallagher provided SandyDuck bed roughness observations. The Field Research Facility, Coastal Engineering Research Center, Duck, North Carolina, provided excellent logistical support, the bathymetric surveys, and 8-m depth pressure array data. A summer course on inverse methods taught by A. F. Bennett served as a springboard for this work.

Gene Terray provided important insight, and John Trowbridge, Dennis McGillicuddy, and two anonymous reviewers provided valuable feedback.

APPENDIX A

Relating Cost-Function Weights to Covariances

Minimization of a cost function [e.g., (3)] is shown to be equivalent to maximum likelihood estimation of a continuous Gaussian random variable and that the weight in the cost function [e.g., $C_{f_x}^{-1}$ in (3)] represents the inverse covariance. The nondegenerate and continuous, symmetric, positive definite kernel $C(x, x')$ is decomposed into (cf. Courant and Hilbert 1953)

$$C(x, x') = \sum_{l=1}^{\infty} \hat{c}_l g_l(x) g_l(x'),$$

where the $\hat{c}_l$ and $g_l(x)$ are the eigenvalues (real and >0) and (orthogonal) eigenfunctions of $C(x, x')$. Orthogonality is defined as

$$\int_0^L g_l(x) g_m(x)\, dx = \delta_{lm},$$

where L is the domain size and δ_{lm} is the Kronecker delta function. For the set of continuous functions, the $g_l(x)$ provide a basis set. If $C(x, x')$ were a function of $x - x'$ only (i.e., homogeneous), then the g_l are complex exponentials. The inverse of $C(x, x')$ is

$$C^{-1}(x, x') = \sum_{l=1}^{\infty} \hat{c}_l^{-1} g_l(x) g_l(x').$$

The basis set also decomposes the random function $f(x)$,

$$f(x) = \sum_{l=1}^{\infty} \hat{f}_l g_l(x). \tag{A1}$$

Substituting the decompositions for $f(x)$ and $C(x, x')$ into a cost-function-type integral results in

$$\int\int_0^L f(x') C^{-1}(x, x') f(x')\, dx'\, dx = \sum_{l=1}^{\infty} \hat{f}_l^2 \hat{c}_l^{-1}. \tag{A2}$$

The expression (A2) is the argument in the exponential for an infinite set of independent zero-mean Gaussian random variables $\hat{f}_l$ with probability density function

$$P(\hat{f}_l) = \frac{1}{\sqrt{2\pi}\hat{c}_l} \exp\left(-\frac{\hat{f}_l^2}{2\hat{c}_l}\right).$$

With the continuous random function $f(x)$ decomposed into an infinite sum of independent zero-mean Gaussian random variables $\hat{f}_l$, it is straightforward to demonstrate that $E[f(x)] = 0$:

$$E[f(x)] = \sum_{l=1}^{\infty} E(\hat{f}_l) g_l(x) \quad \text{and}$$

$$E[\hat{f}_l] = \prod_{n=1}^{\infty} \int_{-\infty}^{\infty} \frac{\hat{f}_l}{2\pi\hat{c}_n} \exp\left(-\frac{1}{2}\hat{f}_n^2 \hat{c}_n^{-1}\right) d\hat{f}_n = 0;$$

thus, $E[f(x)] = 0$ as well. The covariance of the random function $f(x)$, defined as $E[f(x) f(x')]$, is

$$E[f(x) f(x')] = \sum_{l,m=1}^{\infty} E[\hat{f}_l \hat{f}_m] g_l(x) g_m(x'). \tag{A3}$$

Expanding $E[\hat{f}_l \hat{f}_m]$,

$$E[\hat{f}_l \hat{f}_m] = \prod_{n=1}^{\infty} \int_{-\infty}^{\infty} \frac{\hat{f}_l \hat{f}_m}{2\pi\hat{c}_n} \exp\left(-\frac{1}{2}\hat{f}_n^2 \hat{c}_n^{-1}\right) d\hat{f}_n = \hat{c}_l \delta_{lm},$$

and substituting into (A3) yields

$$E[f(x) f(x')] = C(x, x').$$

Thus, cost-function (weighted by an inverse covariance) minimization is equivalent to maximum likelihood estimation of a continuous random function.

APPENDIX B

Consistency Checks with Prior Assumptions

The hypothesis that the difference ($\delta\overline{v}$) between inverse $\overline{v}$ (or also setup $\overline{\eta}$) solutions and data

$$\delta\overline{v}_n = \overline{v}^{(i)}(x_n) - d_n^{(\overline{v})}$$

are (N) samples from a zero-mean Gaussian random variable with prior data variance $\sigma_{\overline{v}d}^2$ is tested. If the inverse solution is not consistent with the prior data variance, it should be rejected. Consider first the sample variance var($\delta\overline{v}$). If this hypothesis is true, then with 95% probability the true variance falls within

$$\frac{(N-1)\ \text{var}(\delta\overline{v})}{\chi_{N-1}^2(0.025)} - \frac{(N-1)\ \text{var}(\delta\overline{v})}{\chi_{N-1}^2(0.975)},$$

where $\chi_{N-1}^2(y)$ represents the location where the chi-squared cumulative distribution function (cdf) with $N - 1$ degrees of freedom equals the probability y. If this confidence interval does not contain the prior $\sigma_{\overline{v}d}^2$, then it should be rejected. Similarly, the 95% confidence limits on the sample mean $\langle\delta\overline{v}\rangle$ are given by a Student's t distribution with $N - 1$ degrees of freedom. If the interval

$$\langle\delta\overline{v}\rangle \pm t_{N-1}(0.025)\sqrt{\frac{\text{var}(\delta\overline{v})}{N}}$$

[where $t_M(y)$ is the location where the Student's t cdf equals probability y] does not contain zero, then the inverse solution is not consistent with the zero-mean data error and also should be rejected.

Similar consistency checks are performed for the inverse solutions for the forcing and c_d error. The contin-

uous functions (e.g., f_x) are decomposed into Fourier coefficients [e.g., (A1)] using the basis functions of their respective prior covariances. Each Fourier coefficient ($\hat{f}_l$) is then a sample from a zero-mean Gaussian random variable with variance given by the prior covariance eigenvalue (i.e., $\hat{c}_l$). If these hypotheses are correct, then the statistics (summed over the number of data N)

$$\sum_{l=1}^{N} \hat{f}_l \quad \text{and} \quad \sum_{l=1}^{N} \frac{\hat{f}_l^2}{\hat{c}_l}$$

are zero-mean Gaussian random variables with variance $\Sigma_{l=1}^{N} \hat{c}_l$ and a ($N - 1$ degrees of freedom) chi-squared random variable, respectively. The significance tests described for the data are applied to test whether the inverse forcing error or c_d error are consistent with the prior assumptions. The sum is over N (instead of ∞) because with finite data only a finite amount of information (i.e., approximately the first N Fourier coefficients) is added.

REFERENCES

Battjes, J. A., 1975: Modeling of turbulence in the surfzone. *Proc. Symp. on Modeling Techniques*, San Fransisco, CA, ASCE, 1050–1061.

——, and M. J. F. Stive, 1985: Calibration and verification of a dissipation model for random breaking waves. *J. Geophys. Res.*, **90,** 9159–9167.

Bennett, A. F., 1992: *Inverse Methods in Physical Oceanography*. Cambridge University Press, 346 pp.

Bowen, A. J., D. L. Inman, and V. P. Simmons, 1968: Wave ''set-down'' and set-up. *J. Geophys. Res.*, **73,** 2569–2577.

Brethereton, F. P., R. E. Davis, and C. B. Fandry, 1976: A technique for objective analysis of oceanographic experiments applied to MODE-73. *Deep-Sea Res.*, **23,** 559–582.

Church, J. C., and E. B. Thornton, 1993: Effects of breaking wave induced turbulence within a longshore current model. *Coastal Eng.*, **20,** 1–28.

Courant, R., and D. Hilbert, 1953: *Methods of Mathematical Physics*. Vol 1. Wiley-Interscience, 560 pp.

Duncan, J. H., 1981: An experimental investigation of breaking waves produced by a towed hydrofoil. *Proc. Roy. Soc. London*, **377A,** 331–348.

Elgar, S., R. T. Guza, B. Raubenheimer, T. H. C. Herbers, and E. L. Gallagher, 1997: Spectral evolution of shoaling and breaking waves on a barred beach. *J. Geophys. Res.*, **102,** 15 797–15 805.

——, ——, W. C. O'Reilly, B. Raubenheimer, and T. H. C. Herbers, 2001: Wave energy and direction observed near a pier. *J. Waterw. Port Coastal Ocean Eng.*, **127,** 2–6.

Feddersen, F., and R. T. Guza, 2003: Observations of nearshore circulation: Alongshore uniformity. *J. Geophys. Res.*, **108**, 3006, doi:10.1029/2001JC001293.

——, ——, S. Elgar, and T. H. C. Herbers, 1998: Alongshore momentum balances in the nearshore. *J. Geophys. Res.*, **103,** 15 667–15 676.

——, ——, S. Elgar, and T. H. C. Herbers, 2000: Velocity moments in alongshore bottom stress parameterizations. *J. Geophys. Res.*, **105,** 8673–8686.

——, E. L. Gallagher, S. Elgar, and R. T. Guza, 2003: The drag coefficient, bottom roughness, and wave-breaking in the nearshore. *Coastal Eng.*, **48,** 189–195.

Gallagher, E. L., E. B. Thornton, and T. P. Stanton, 2003: Sand bed roughness in the nearshore. *J. Geophys. Res.*, **108**, 3039, doi: 10.1029/2001JC001081.

Garcez-Faria, A. F., E. B. Thornton, T. P. Stanton, C. M. Soares, and T. C. Lippmann, 1998: Vertical profiles of longshore currents and related bed shear stress and bottom roughness. *J. Geophys. Res.*, **103,** 3217–3232.

Lentz, S. J., R. T. Guza, and S. Elgar, 2003: Observations of the flow field near the nose of a buoyant coastal current. *J. Phys. Oceanogr.*, **33,** 933–943.

Lippmann, T. C., T. H. C. Herbers, and E. B. Thornton, 1999: Gravity and shear wave contributions to nearshore infragravity motions. *J. Phys. Oceanogr.*, **29,** 231–239.

Longuet-Higgins, M. S., 1970: Longshore currents generated by obliquely incident sea waves 1. *J. Geophys. Res.*, **75,** 6790–6801.

——, and R. W. Stewart, 1964: Radiation stress in water waves, a physical discussion with application. *Deep-Sea Res.*, **11,** 529–563.

Noyes, T. J., R. T. Guza, S. Elgar, and T. H. C. Herbers, 2004: Field observations of shear waves in the surf zone. *J. Geophys. Res.*, **109,** C01031, doi:10.1029/2002JC001761.

Özkan-Haller, H. T., and J. T. Kirby, 1999: Nonlinear evolution of shear instabilities of the longshore current: A comparison of observations and computations. *J. Geophys. Res.*, **104,** 25 953–25 984.

Raubenheimer, B., R. T. Guza, and S. Elgar, 2001: Field observations of wave-driven setdown and setup. *J. Geophys. Res.*, **106,** 4629–4638.

Reniers, A. J., and J. A. Battjes, 1997: A laboratory study of longshore currents over barred and non-barred beaches. *Coastal Eng.*, **30,** 1–22.

Ruessink, B. G., J. R. Miles, F. Feddersen, R. T. Guza, and S. Elgar, 2001: Modeling the alongshore current on barred beaches. *J. Geophys. Res.*, **106,** 22 451–22 463.

Slinn, D. N., J. S. Allen, P. A. Newberger, and R. A. Holman, 1998: Nonlinear shear instabilities of alongshore currents over barred beaches. *J. Geophys. Res.*, **103,** 18 357–18 379.

Stive, M. J. F., and H. J. de Vriend, 1994: Shear stresses and mean flow in shoaling and breaking waves. *Proc. 24th Int. Coastal Engineering. Conf.*, Kobe, Japan, ASCE, 594–608.

Svendsen, I. A., and U. Putrevu, 1994: Nearshore mixing and dispersion. *Proc. Roy. Soc. London*, **445A,** 561–576.

Thornton, E. B., and R. T. Guza, 1983: Transformations of wave height distribution. *J. Geophys. Res.*, **88,** 5925–5938.

——, and ——, 1986: Surf zone longshore currents and random waves: Field data and models. *J. Phys. Oceanogr.*, **16,** 1165–1178.

——, J. L. Swayne, and J. R. Dingler, 1998: Small-scale morphology across the surf zone. *Mar. Geol.*, **145,** 173–196.